

## Anisotropic surface properties of micro/nanostructured a-C:H:F thin films with self-assembly applications

V.-M. Freire, C. Corbella, E. Bertran, S. Portal-Marco, M. Rubio-Roy et al.

Citation: *J. Appl. Phys.* **111**, 124323 (2012); doi: 10.1063/1.4730783

View online: <http://dx.doi.org/10.1063/1.4730783>

View Table of Contents: <http://jap.aip.org/resource/1/JAPIAU/v111/i12>

Published by the [American Institute of Physics](#).

---

### Related Articles

Effect of oxygen deficiency on SrTiO<sub>3</sub>(001) surface reconstructions

*Appl. Phys. Lett.* **100**, 263106 (2012)

The influence of substrate morphology on thickness uniformity and unintentional doping of epitaxial graphene on SiC

*Appl. Phys. Lett.* **100**, 241607 (2012)

Orientation-dependent surface potential behavior in Nb-doped BiFeO<sub>3</sub>

*Appl. Phys. Lett.* **100**, 172901 (2012)

Qualitative determination of surface roughness by in situ reflection high energy electron diffraction

*Appl. Phys. Lett.* **100**, 151604 (2012)

Role of dual-laser ablation in controlling the Pb depletion in epitaxial growth of Pb(Zr<sub>0.52</sub>Ti<sub>0.48</sub>)O<sub>3</sub> thin films with enhanced surface quality and ferroelectric properties

*J. Appl. Phys.* **111**, 064102 (2012)

---

### Additional information on *J. Appl. Phys.*

Journal Homepage: <http://jap.aip.org/>

Journal Information: [http://jap.aip.org/about/about\\_the\\_journal](http://jap.aip.org/about/about_the_journal)

Top downloads: [http://jap.aip.org/features/most\\_downloaded](http://jap.aip.org/features/most_downloaded)

Information for Authors: <http://jap.aip.org/authors>

## ADVERTISEMENT

**AIP Advances**

Special Topic Section:  
**PHYSICS OF CANCER**

Why cancer? Why physics? [View Articles Now](#)

## Anisotropic surface properties of micro/nanostructured a-C:H:F thin films with self-assembly applications

V.-M. Freire,<sup>a)</sup> C. Corbella, E. Bertran, S. Portal-Marco, M. Rubio-Roy, and J.-L. Andújar  
*FEMAN group, IN<sup>2</sup>UB, Departament de Física Aplicada i Òptica, Universitat de Barcelona, Martí i Franquès 1, E08028, Barcelona, Spain*

(Received 15 February 2012; accepted 26 May 2012; published online 26 June 2012)

The singular properties of hydrogenated amorphous carbon (a-C:H) thin films deposited by pulsed DC plasma enhanced chemical vapor deposition (PECVD), such as hardness and wear resistance, make it suitable as protective coating with low surface energy for self-assembly applications. In this paper, we designed fluorine-containing a-C:H (a-C:H:F) nanostructured surfaces and we characterized them for self-assembly applications. Sub-micron patterns were generated on silicon through laser lithography while contact angle measurements, nanotribometer, atomic force microscopy (AFM), and scanning electron microscopy (SEM) were used to characterize the surface. a-C:H:F properties on lithographed surfaces such as hydrophobicity and friction were improved with the proper relative quantity of CH<sub>4</sub> and CHF<sub>3</sub> during deposition, resulting in ultrahydrophobic samples and low friction coefficients. Furthermore, these properties were enhanced along the direction of the lithography patterns (in-plane anisotropy). Finally, self-assembly properties were tested with silica nanoparticles, which were successfully assembled in linear arrays following the generated patterns. Among the main applications, these surfaces could be suitable as particle filter selector and cell colony substrate. © 2012 American Institute of Physics. [<http://dx.doi.org/10.1063/1.4730783>]

### I. INTRODUCTION

Carbon is an abundant element in nature and it constitutes one of the basic elements for life. It is also widely used in industry for materials manufacturing. The fundamental characteristic of carbon is its unique capability for combining with other elements. Due to the variety of possible bonding configurations, carbon has a number of allotropes: graphene, nanotubes, fullerenes, graphite, diamond, and amorphous carbon (a-C and a-C:H).<sup>1,2</sup> Hard a-C thin films, also called DLC, can be deposited by different deposition techniques.<sup>3,4</sup>

Some important applications of DLC surfaces are addressed to magnetic storage technology, automotive industry and injection molding, among others.<sup>4</sup> Some of the main advantages of DLC films are hardness and wear resistance. However, lately there are properties being investigated, such as biocompatibility and antithrombogenicity. Such properties make them candidates for a number of medical applications where wear resistant coatings, such as prosthesis, or simply biocompatible parts are required.<sup>5</sup> The surfaces of the implants are exposed to the interaction with the body cells and fluids and to potentially corrosive medium. These effects can include cellular damage, infections, blood coagulation (potentially leading to thrombosis), and failure of the implants.<sup>6,7</sup> Coating the implants with protective films, which can reduce corrosion and wear, may prevent or alleviate the problems described above and extend the lifetime of implants to the benefit of the patients. DLC, thus, appears to

be an ideal material for such purposes and its use for protecting implants was already suggested in the early 1990s.<sup>8</sup> At present, using cell culture, it is possible to produce a cellular growth, for example, of fibroblasts or osteoblasts attached to a surface by means of a thin film of polylysine. DLC is a suitable candidate due to its bio-properties for building interfaces between a non biological substrate (surface lithographed c-Si) and the cell culture medium.

On the other hand, the introduction of alloying elements in a-C thin films has been used for a long time to improve specific properties of the films depending on the application. Some of the most studied modifications include the reduction of internal compressive stress with N, Si, or metal incorporation; the decrease of surface energy, the reduction of friction coefficient, and the modification of the electrical properties with F, Si-O, and some metals. Al, Fe, Ni, Nb, and Ti, for example, reduce surface free energy (SFE) as measured with contact angle, whereas W slightly increases SFE. Interestingly, addition of both Si and O can reduce the SFE more than only with Si.<sup>9-11</sup> Among these elements, fluorine incorporation leads to the highest water contact angles (>100°) and lowest SFE (~20 mJ/m<sup>2</sup>).<sup>4,12</sup>

Colloidal particles are small objects with at least one characteristic dimension comprised between 1 nm and 1 μm. The most widely studied and used colloidal particles are silica beads and polymer latexes.<sup>13</sup> In the past decades, the formation of highly ordered structures of colloidal particles with sufficiently large domain sizes has attracted a wide research interest, also given the ample range of possible applications for this novel class of materials.<sup>14</sup> Several self-organizing techniques have been devised to assemble high-quality arrays of monodispersed colloids.<sup>15</sup> The synthesis of

<sup>a)</sup>Electronic mail: victor.freire@ub.edu. Tel.: +34 934 039 224. Fax: +34 934 039 219.

colloids of highly uniform size and shape (monodisperse) is very important for the self-assembly of crystalline arrays in large areas, since uniformity and order affect the electronic, optical, magnetic, and electrokinetic properties of the resulting aggregates.<sup>13</sup> Arrangement and adhesion of these silica particles will depend on the chemical state of the surface and its topography. In this first work, nanoparticles would be like “inert cells” in order to test a-C:H:F surface properties.

The present work aims at designing and fabricating nano/micrometric structures by laser lithography directly on silicon wafers, which have been coated later with a a-C:H:F thin film with its surface and tribological characterization. As a beginning, the carbon coated lithographed structure will be tested using silica sub-micron particles to determine if they form arrays.

## II. EXPERIMENTAL METHODS

### A. Lithography technique

Surface patterning was performed through laser lithography using a Mask Plotter, DWL66 Heidelberg Instruments model, installed at the *Parc Científic de Barcelona* (PCB-UB). The Mask Plotter can fabricate high resolution masks directly patterning substrates for photolithography uses; lateral resolution goes down to 0.5  $\mu\text{m}$ . This technique is advantageous to pattern sub-micrometric structures in very large areas in much shorter time than using electron beam lithography. An Oxford Plasmalab 80 (PCB-UB) was used to etch the silicon surface. The reactive ion etching (RIE) process was carried out with a total gas flow of 50 sccm of HBr, at a pressure of 30 mTorr and 250 W of power, during 10 min. The etch rate was 40 nm/min.

In this earlier phase, we intend to produce suitable substrates for controlling self-assembly experiments with inorganic nanoparticles. So, in this work, we propose some particular structures consisting in tracks  $2 \pm 0.5 \mu\text{m}$  wide and with different separation among themselves of 0.5, 1, 2, and

3  $\mu\text{m}$ . In spite of some deviations, the reproducibility of the nanostructures was good enough to carry on the experiments. Designed with the program CLEWIN 4<sup>®</sup>, we lithographed areas of about 4 cm<sup>2</sup>. These areas provided enough space to do all the characterization.

### B. Deposition conditions

a-C:H:F thin films were deposited using PECVD technology powered with bipolar pulsed DC energy. The PECVD processes were carried out in a computer-controlled plasma reactor named PEDRO (Plasma Etching and Deposition ReactOr) (Fig. 1). Apart from the PECVD, other techniques are available in the reactor: magnetron sputtering, RIE, and ion beam etching (IBE). PEDRO has a main spherical vacuum chamber of 80 l of volume and three load-lock chambers to insert the samples and/or the cathodes. The reactor is pumped down by means of a turbomolecular pump, and the load-lock chambers are evacuated by rough pumping (low vacuum). With this system, a base pressure of  $10^{-5}$  Pa can be achieved. The cathodes can be connected to a high power supply to drive the voltage needed to switch on and maintain the plasma. Gas valves, pressure gauges, and mass flow controllers are operated with a LABVIEW<sup>®</sup> interface, which can be programmed for the deposition process.

Methane<sup>16</sup> (CH<sub>4</sub>) and trifluoromethane (CHF<sub>3</sub>) were used as film precursors. However, it is very difficult to deposit fluorinated carbon on silicon because of adhesion problems on the substrate. Thus, a thin buffer layer of a-C:H was previously deposited to improve a-C:H:F film adhesion. The deposition of all the films was done at 10 Pa in power regulation mode at 57 W, which provided a negative peak voltage close to 1000 V. This voltage peak yields an approximate power of 1.3 W/cm<sup>2</sup>. Moreover, pulse frequency and duty cycle were fixed to 100 kHz and 80%, respectively. These conditions were previously observed to produce DLC films with average characteristics.<sup>1,17</sup> In a preliminary study,

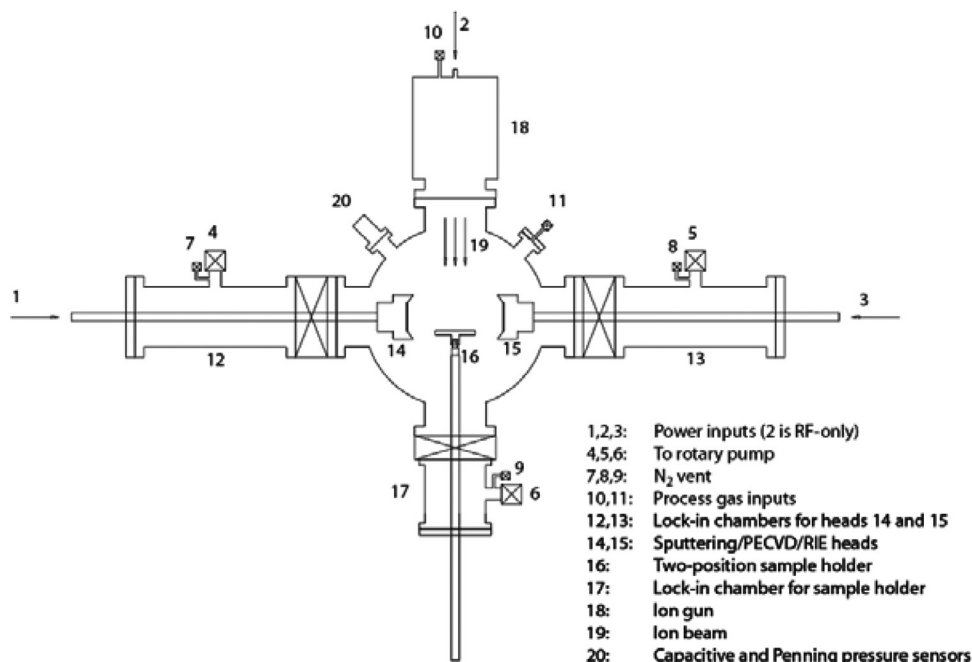


FIG. 1. Schematic figure of PEDRO. Several techniques can be used: PECVD, magnetron sputtering, RIE, and IBE.

a-C:H:F films were grown on flat substrates. The  $\text{CHF}_3$  relative flow was set to 50%, 75%, 85%, and 90% versus total mix of gases ( $\text{CH}_4 + \text{CHF}_3$  at total gas flow of 25 sccm), to study the effects of the progressive fluorination of the films. The results of such studies are published elsewhere<sup>4,12</sup> and are summarized in Table I. The optimal gas combination, regarding contact angle and friction coefficient, was used to coat the nanostructured surfaces. These layers were deposited varying gradually the concentration of the precursor gases until the desired relative gas flow was achieved.

Outline of the deposition process: (1) start: only methane without discharge (120 s), (2) buffer layer: methane plasma (60 s), (3) gradient interface: gradient between  $\text{CH}_4$  and  $\text{CHF}_3$  flows with plasma (60 s); (4) stabilized proportion of gases with plasma (60 s). A total time process of 5 min was set, previously calculated to obtain a thin film of approximately 100 nm. Substrate was kept at room temperature by means of a water-cooling circuit, in order to grow amorphous films.

### C. Characterization

One of the first steps was measuring the thickness of the films. Profilometry was carried out with a Dektak 3030. A stylus scans the surface with nanometric precision in depth as we are interested in 100 nm thick films.

Wettability, which plays an important role in surfaces addressed to biomedical applications, was characterized with a contact angle goniometer CAM 200 from KSV. This instrument is equipped with a multidispenser system that provided drops of deionised water. Pictures were captured with a camera in either static or advancing (dynamic) mode.

Another important point is the friction and hardness of the film. In this occasion, we used a nanotribometer from CSM with a product-integral-derivative (PID) humidity controller, which measured friction coefficient. It consists in a sliding WC ball (3 mm diameter) that scratches the surface in linear reciprocating mode. The applied load, 100 mN, was low enough to perform scans without damaging significantly the surface pattern. Every sample took an average of 2 h in every direction, orthogonal and parallel to the lithography, with a mean velocity of 1 mm/s. The experiments were done at a temperature of about 27 °C and a constant relative humidity of 40%.

A first approach to characterize the surface topography consisted in an optical microscopy study of the samples: an Inspection Jenatech microscope and an Optical Imaging Profiler PL $\mu$  2300 from Sensofar in interferometric and confocal

TABLE I. Preliminary results of the progressive fluorination of the films (relative quantity of  $\text{CHF}_3$ ) deposited on flat c-Si wafers, looking for the best compromise between contact angle (biggest) and friction coefficient (lowest), which is 90% of  $\text{CHF}_3$  respect to the total flow of gas in the reactor.

Relative quantity of $\text{CHF}_3$ (sample)	Contact angle (°)	Friction coefficient $\mu$
50% (10G1901)	76.66	0.20
75% (10G2201)	76.69	0.20–0.21
85% (10G2302)	77.36	0.20–0.21
90% (10G2601)	78.87	0.23–0.24

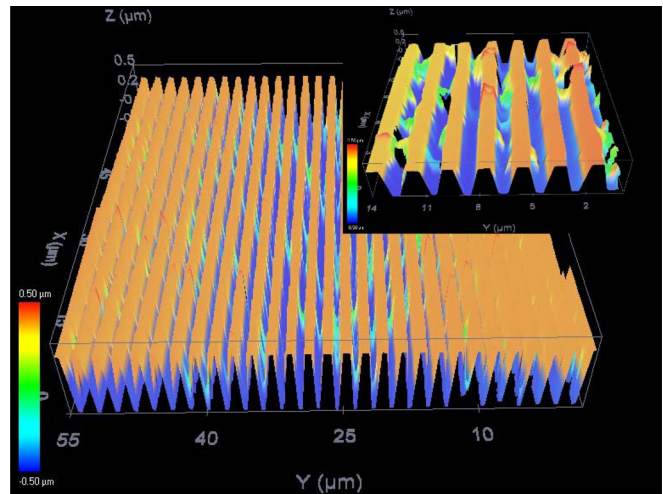


FIG. 2. Confocal/interferometric 3D images of the self-assembly test on sample "D," 2  $\mu\text{m}$  width pattern, and a separation of 2  $\mu\text{m}$ . Green and yellow spots in the valleys represent silica nanoparticles.

modes to increase image resolution (Fig. 2). High resolution scanning electron microscopy (HR-SEM) observations were performed in order to characterize the morphology of the lithographed structures and their final view with the attached  $\text{SiO}_2$  nanoparticles (Fig. 3). A field emission microscope Strata DB235 from FEI Company (installed at PCB-UB) and a Hitachi FE S-4100 SEM (installed at SCT-UB) were used for this purpose.

Finally, in order to get accurate height profiles, we used a Park XE-70 (AFM) in non-contact mode to measure surface topography. We also used an AFM Multimode from Veeco (SCT-UB) operated in contact mode. We need the real heights of the lithographed tracks to compare them after being coated with the fluorinated carbon film.

### D. Silica nanoparticles

The synthesis of spherical silica particles ( $\text{SiO}_2$ ) was carried out by sol-gel method with a precursor of tetraethylorthosilicate (TEOS, high purity  $\geq 99.0\%$ , Fluka). Hydrolysis and condensation reactions were initiated by the addition of water diluted in ethanol. A small concentration of ammonia ( $\text{NH}_4\text{OH}$ , 25%, Merck) in the solution fixed the pH to basic. After stirring for a short time, the solution turned white which is the sign that the average size of particles or their aggregates achieved the wavelength region of visible light. After 1 h, the particles reached their final size. Finally, the residual chemicals were eliminated by centrifugation before collection of the sol-gel sub-micron particles and redispersion in fresh ethanol. The solution contained particles showing a very narrow size distribution (monodisperse) with an average size of 400 nm.<sup>14,15</sup>

## III. RESULTS AND DISCUSSION

### A. Deposition conditions

The physical properties of the carbon layers depend directly on the deposition parameters. Before depositing the a-C:H:F films on the lithographed silicon, we optimized the

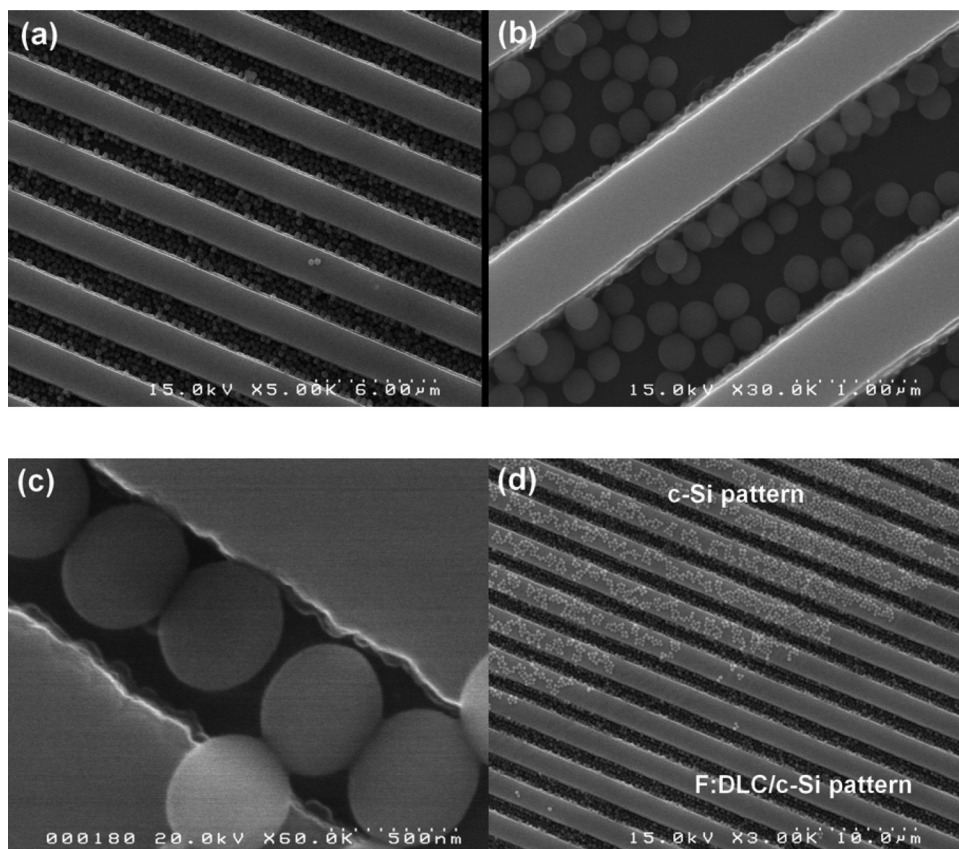


FIG. 3. SEM images of the self-assembly test, where almost all the particles are inside the micro/nanostructures; samples with a separation pattern of  $1\ \mu\text{m}$  (a) and (d),  $2\ \mu\text{m}$  (b) and  $0.5\ \mu\text{m}$  (c). Notice that different surface film has different particle attachment, different wettability.

relative quantity of  $\text{CHF}_3$  versus  $\text{CH}_4$  in depositions on flat silicon wafers. The parameters to optimize are contact angle and friction coefficient. After four tests with different concentrations, we did the respective measurements in contact angle and nanotribometer (see Table I). The deposition process with a 90% of  $\text{CHF}_3$  and a 10% of  $\text{CH}_4$  respect the total mixture provided to the sample the best compromise between tribology and wettability, high contact angle values and still a low friction coefficient. Furthermore, beyond the 90% of  $\text{CHF}_3$ , the ratio F/C exceeds 0.5, so there are more fluorine atoms than carbon atoms;<sup>4</sup> it decreases the stress at the expense of mechanical resistance with probably less C–C bonds, so the  $\text{sp}^2$  and  $\text{sp}^3$  structures disappear and the film gets unstable and unstructured. Therefore, lithographed samples were coated with 90% of  $\text{CHF}_3$  in the precursor. Total deposition time was 5 min long in order to obtain a thin film layer of about 100 nm thick, thin enough to preserve/reproduce the topography of the substrate and thick enough for its protective performance.

## B. Surface morphology

AFM images were obtained before and after the fluorinated carbon deposition on the lithographed samples in  $5 \times 5$  and  $10 \times 10\ \mu\text{m}^2$  areas, in order to check the change in topography due to the deposition of a-C:H:F films. In both cases, the depth of the lithographed tracks was approximately the same, around 400 nm. In most of cases, the angles of the trenches were about  $65^\circ$ – $70^\circ$  in one side of the trench and  $\sim 60^\circ$  on the other. The RMS roughness was essentially the same on the top and bottom of the structure (8 nm and

7–8 nm, respectively). We could also see that the deposition process kept the shape of the lithography, so we can say that it is a conformal process (Figs. 4(c) and 4(d)).

## C. Contact angle

In the static mode, the needle provides individual droplets with a fixed volume. We used water drops of 10–15  $\mu\text{l}$  of water. We did all the experiments at around  $25^\circ\text{C}$  and at a relative humidity of 50%. We measured the contact angle on 3 parts of every sample and the final values were calculated through an arithmetic mean (Table II).

As we see in Figs. 5(b) and 5(c), the difference in the contact angle of the droplet between the two directions (orthogonal and parallel) is significant, indicating a large in-plane anisotropy which modifies the shape of the droplet.<sup>18</sup> We can consider that the droplet is deposited on the micro/nanostructures, which behave like pillars; the advancing edges in the orthogonal direction of the lithography undergo a certain resistance in spreading due to the interface pinning effect. The wetting mode in the parallel direction behaves like on flat surfaces. Thus, the equilibrium shape obtained is the local minimum of the free energy and it satisfies the condition that the mean curvature of the surface is constant. The local contact angle along the actual solid-liquid-air contact line is equal to the intrinsic contact angle.<sup>19,20</sup> It also increased substantially after the deposition process. That means that fluorinated carbon films are quite hydrophobic.

The most interesting part of the experiment was the advancing mode (Fig. 5(a)). In this case, the needle is really close to the surface of the sample and it feeds water to the

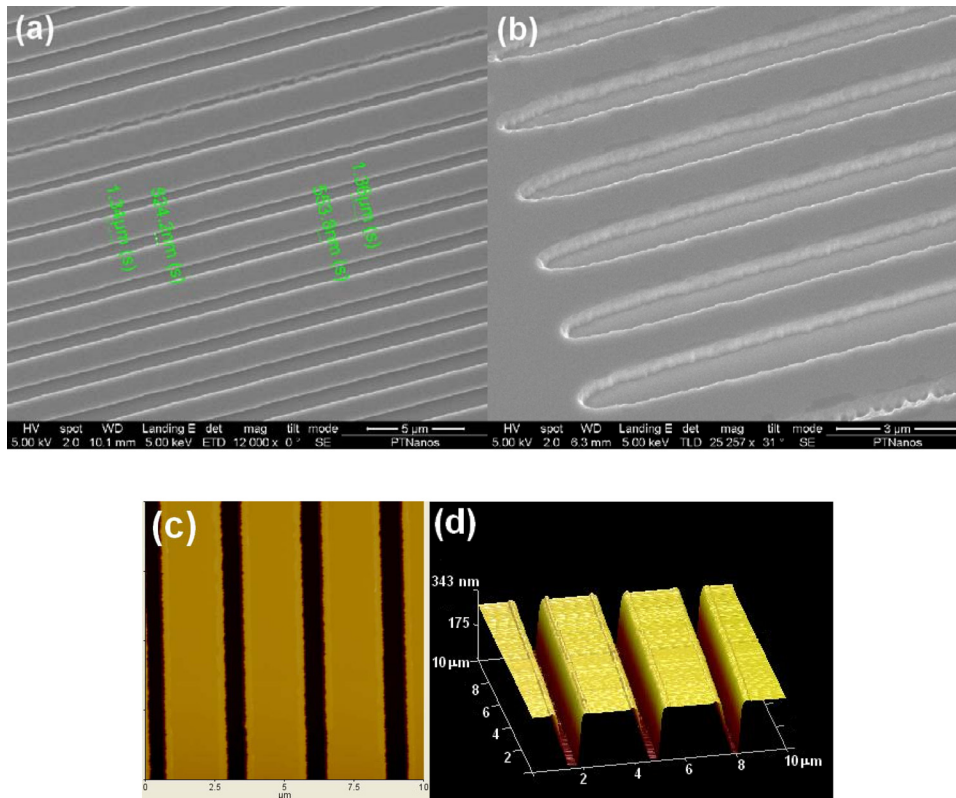


FIG. 4. HR-SEM images of lithographed silicon of the sample “#1,” 2  $\mu\text{m}$  width and 0.5  $\mu\text{m}$  of separation (a) and (b). AFM images of the lithographed surface of the same sample before the fluorine-carbon deposition (c) and after (d) in order to check that, actually, it is a conformal process.

drop with a continuous flow. On the other hand, while on receding mode the needle sucks water from the drop. In this configuration, we could observe that contact angle increased dramatically with respect to the static mode operation. This behaviour indicates a probable time-dependence of the contact angle, which has time to relax on the static case. In this way, we achieved contact angles very close to  $180^\circ$ , superhydrophobicity (or even ultrahydrophobicity); defined as high contact angles ( $>150^\circ$ ) and low contact angle hysteresis ( $<10^\circ$ ),<sup>21</sup> which gives a measure of surface stickiness too. The static mode is a more distorted measurement because it depends on the height of the needle; when the droplet falls, it is flattened against the surface. This is why we consider that the best method is the advancing mode with a slow enough speed. While parallel contact angle values maintained almost constant versus the separation pattern, the orthogonal contact angle seemed to be dependent on this; when the distance of the tracks increases, the contact angle decreases (Fig. 5(a)).

Wenzel and Cassie-Baxter are the two main models that attempt to describe the wetting of textured surfaces. While in Wenzel model the drop wets the entire solid surface area

( $\cos\theta_W = r\cos\theta_0$ ), a more complex behavior is described by Cassie-Baxter, with air trapped between the drop and the structured surface ( $\cos\theta_W = r \cdot f\cos\theta_0 + f - 1$ ). Where  $\theta_W$  is the apparent contact angle,  $\theta_0$  is the contact angle on a flat surface,  $r$  is the roughness ratio, and  $f$  is the fraction of the projected area of the solid surface that is wetted by the liquid.<sup>21,22</sup> A few calculations evidenced that the model that best fits the experimental data is the Cassie-Baxter model, with air trapped between the drop and the surface.

#### D. Nanotribometer

Figures 6(a) and 6(c) show the friction coefficient along the cycles with a double line graphic: one line represents the scan forward and the other line the scan backward. As reported elsewhere,<sup>23</sup> the curve is divided into three sections: running-in period, transition regime, and steady state. The variations in the first stage are ascribed to surface ploughing and mechanically induced desorption of hydrogen. During the transient regime, surface modification conformal to the ball shape took place, as well as interactions with wear particles.

TABLE II. Main characteristics of the four different types of samples done in this work: lithography patterns, wettability and hardness. In order to compare them, the values in a flat silicon surface for contact angle and friction coefficient are  $87.4^\circ$  and  $\sim 0.24$  respectively.

Sample	Width ( $\mu\text{m}$ )	Separation ( $\mu\text{m}$ )	Contact angle, parallel ( $^\circ$ ) (advancing mode)	Contact angle, orthogonal ( $^\circ$ ) (advancing mode)	Friction coefficient $\mu$ (parallel)	Friction coefficient $\mu$ (orthogonal)
10G2701 (#1)	2	0.5	85.5	166.3	0.12	0.13
10G2704 (I)	2	1	84.1	150.8	0.15	0.27
10G2703 (D)	2	2	88.4	133.5	0.21	0.13
10G2702 (SP)	2	3	90.1	141.3	0.22	0.21

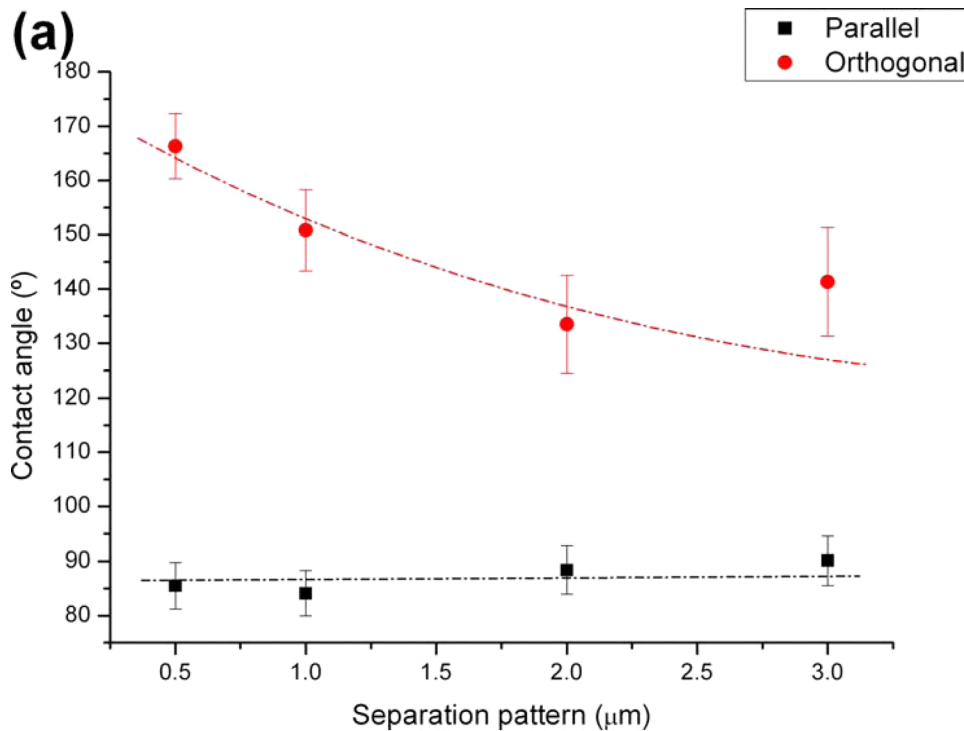
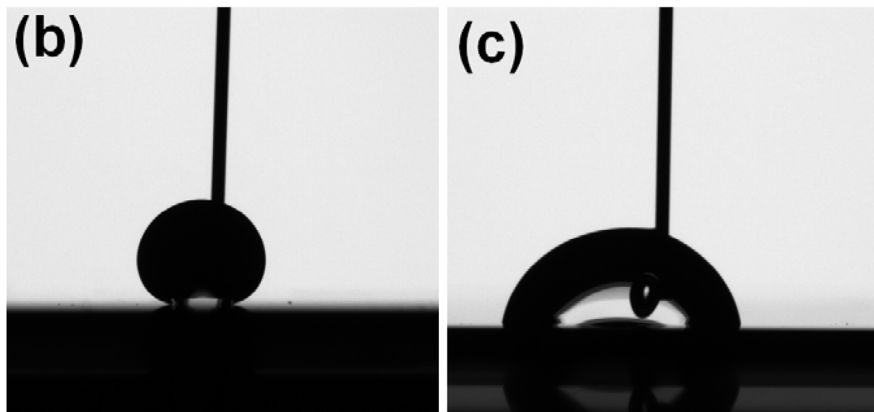


FIG. 5. Plot of the contact angle in advancing mode, orthogonal and parallel to the lithography, versus distance between tracks (a). Images of water droplets orthogonal (b) and parallel (c) to the lithography in advancing mode of the sample “#1” ( $2\ \mu\text{m}$  width tracks with a separation of  $0.5\ \mu\text{m}$ ). Notice that orthogonal mode (b) shows ultrahydrophobic character.



In the case of structured a-C:H:F samples, they achieved lower and more stable values than in the flat a-C:H:F coating samples, with friction coefficients of  $\sim 0.24$  (Table II). The sporadic spikes underwent by the friction coefficient during the cycles could come from momentary interactions of the wear particles with the ball of the nanotribometer. These particles, which are debris removed from the sample during the tests, contribute to enhance the friction via several mechanisms, as for instance dragging, ploughing, or adhesion.

We also noticed a different behavior between orthogonal and parallel directions.<sup>18,24</sup> While orthogonal tribology was more stable, the parallel one was more irregular (Figs. 6(a) and 6(c)). A possible reason could be that when the ball scratches parallel to the lithography, the debris produced by the ball remain in the channel and the interaction with the ball affects the measurement. On the other hand, when the ball scratches orthogonally, the debris particles are more easily removed to both sides of the channel and through the valleys of the lithography. So, the channel is surely cleaner and the values are more stable (Fig. 6(b)).

The wear effects of the track of the nanotribometer WC ball on the surface were observed with an optical microscope (Figs. 6(b) and 6(d)). We can notice the differences between the orthogonal and parallel paths. The damage of the surface seemed to be more important in the orthogonal case, but the amount of debris and wear particles was lower. The estimation of wear rate ( $W = V/F \cdot l$ ) also evidenced a small difference between the orthogonal and the parallel wear, which were  $1.8 \times 10^{-6}$  and  $1.2 \times 10^{-6}$   $\text{mm}^3/\text{Nm}$ , respectively.

### E. Silica nanoparticles and arrays

Silica nanoparticles had an average size of 400 nm, ideal for our purpose regarding the dimensions of the lithography. The particles wiping process involved pouring the solution homogeneously on the lithographed surface with two clean coverglasses with scotch tape orthogonally to the direction of the tracks. In this way, we obtained a monolayer of silica particles.

The optical imaging profiler provided the first results of the silica nanoparticles self-assembly (Fig. 2). It clearly

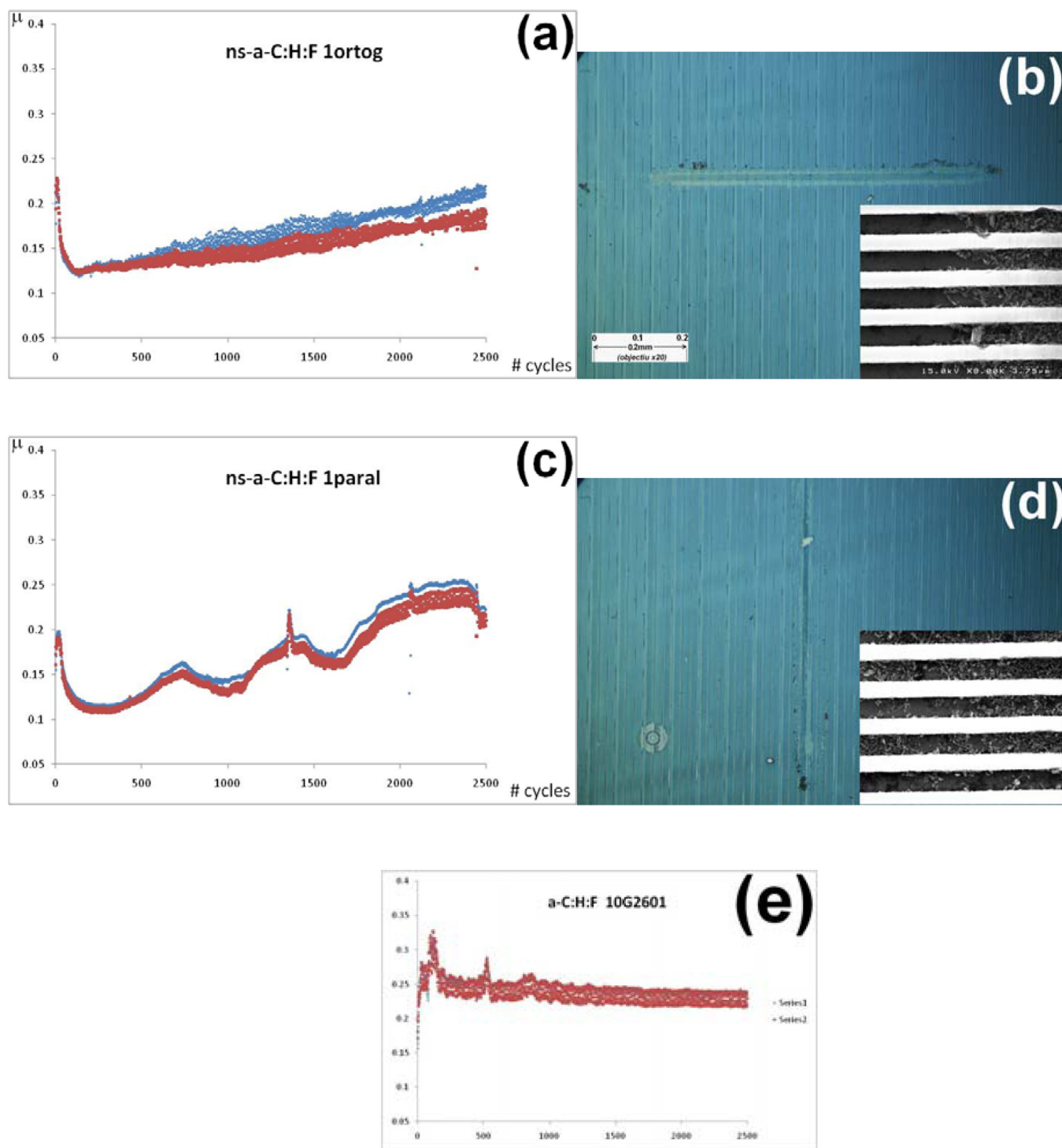


FIG. 6. Plots of the friction coefficient versus number of cycles of sample “#1” ( $2\ \mu\text{m}$  width with a  $0.5\ \mu\text{m}$  of separation) orthogonal (a) and parallel (c) to the lithography. Details of the destruction of the same sample, orthogonal (b) and parallel (d) to the lithography. Last plot (e) shows the friction coefficient in a flat surface; notice that lithography friction is lower than the flat ones, which is typically  $\sim 0.24$ .

shows the pattern of the surface and the silica particles attached to them. In Fig. 2, green/yellow spots inside the pattern correspond to the nanoparticles. We also could see that bigger silica clusters did not fall into the valleys.

SEM imaging (Fig. 3) revealed an almost complete insertion of the spherical nanoparticles inside the valleys, which formed aligned rows and underlying the importance of the surface film, especially in Fig. 3(d). The size of the particles was very homogeneous, around  $400\ \text{nm}$ , which

helped us to identify the width of the valley. The number of particles inside was one or two in width depending on the valley. Regarding to the depth of the valley, the number of particles was also one or two at maximum. So, the bigger the valley was, the more particles were deposited inside. The alignment could be improved by increasing the width of the valleys of the lithography and the separation between tracks and by spreading the particles more carefully. The physical mechanism of self-assembly can be explained by a sum of

different factors: gravitational potential energy minimization (the particles go where the energy is lowest), the nanostructures geometry, the coverglass wiping movement and, once the solvent of the nanoparticles solution dries, Van der Waals forces (physisorption). These results show the feasibility of these nanostructures as a particle filter selector, where only the particles with the same or smaller size than the structures would remain, or a cell colony substrate, where cells can only grow in one direction.

#### IV. CONCLUSIONS

Submicron structures were successfully fabricated by laser lithography and coated with a-C:H:F. Their morphology was characterized by AFM and SEM, whereas their surface properties were studied by nanotribometry and contact angle goniometry. The best tribological (lowest friction coefficient) and wettability (highest contact angle) properties were met when performing the deposition process with 90% CHF<sub>3</sub> and 10% CH<sub>4</sub> of total gas flow. In that case, a-C:H:F films showed hydrophobic character when measuring the contact angle in *static mode*, achieving ultrahydrophobicity in *advancing mode*. Furthermore, there was a big anisotropy between parallel and orthogonal directions to the lithographed tracks. The patterns in the surface seemed to increase the contact angle too. In the tribological studies, the presence of fluorine keeps the friction coefficient at low values, the first laps of the lithographed samples had a very low friction coefficient, just the opposite to the flat ones, which had an initial high peak. Moreover, there were differences between the orthogonal scan, quite homogeneous, and the parallel scan, more irregular. In average, we noticed a lower friction coefficient with lithographed surface. Regarding self-assembly, a lithographed surface has a positive influence on silica nanoparticles, which were arranged following the patterns successfully. The quantity of particles was found to be higher in wide tracks rather than narrow ones. In addition, bigger particles or clusters found more difficulty to attach to the tracks than smaller ones.

#### ACKNOWLEDGMENTS

The authors thank *Generalitat de Catalunya* for financial support of project 2009SGR00185 and *MICINN* of Spanish Government for financial support of project DPI2007-61349, *SCT-UB* for AFM and SEM measures, *PCB-UB* for laser lithography and etching, Josep Ingla for his help with the measures. Carles Corbella thanks *MICINN* for the granting of a *Juan de la Cierva* contract.

- <sup>1</sup>C. Corbella, "Thin film structures of diamond-like carbon prepared by pulsed plasma techniques," Ph.D. dissertation, Universitat de Barcelona, 2005.
- <sup>2</sup>A. C. Ferrari, S. E. Rodil, J. Robertson, and W. I. Milne, *Diamond Relat. Mater.* **11**, 994–999 (2002).
- <sup>3</sup>J. Robertson, *Mater. Sci. Eng. R* **37**, 129–281 (2002).
- <sup>4</sup>M. Rubio-Roy, "Surface properties of hard fluorinated amorphous carbon films deposited by pulsed DC discharges." Ph.D. dissertation, Universitat de Barcelona, 2010.
- <sup>5</sup>R. K. Roy and K-R. Lee, *J. Biomed. Mater. Res. B Appl. Biomater.* **83**, 72–84 (2007).
- <sup>6</sup>A. Grill, *Diamond Relat. Mater.* **12**, 166–170 (2003).
- <sup>7</sup>R. Hauert, *Diamond Relat. Mater.* **12**, 583–589 (2003).
- <sup>8</sup>W. J. Ma *et al.*, *Biomaterials* **28**, 1620–1628 (2007).
- <sup>9</sup>M. Grischke *et al.*, *Diamond Relat. Mater.* **7**, 454–458 (1998).
- <sup>10</sup>R. Hauert, *Tribol. Int.* **37**, 991–1003 (2004).
- <sup>11</sup>S. C. Trippe *et al.*, *Thin Solid Films* **446**, 85–90 (2004).
- <sup>12</sup>M. Rubio-Roy *et al.*, *Diamond Relat. Mater.* **18**, 923 (2009).
- <sup>13</sup>M. Mastrangeli *et al.*, *J. Micromech. Microeng.* **19**, 083001 (2009).
- <sup>14</sup>S. Portal-Marco *et al.*, *Thin Solid Films* **518**, 1543–1548 (2009).
- <sup>15</sup>S-M. Young *et al.*, *Small* **2**(4) 458–475 (2006).
- <sup>16</sup>S. Peter *et al.*, *J. Appl. Phys.* **102**, 053304 (2007).
- <sup>17</sup>C. Corbella, M. Rubio-Roy, E. Bertran, and J. L. Andújar, *J. Appl. Phys.* **106**, 033302 (2009).
- <sup>18</sup>C. Corbella, S. Portal-Marco, M. Rubio-Roy, E. Bertran, G. Oncins, M. A. Vallvé, J. Ignés-Mullol, and J.-L. Andújar, *J. Phys. D: Appl. Phys.* **44**, 395301 (2011).
- <sup>19</sup>Y. Chen *et al.*, *J. Colloid Interface Sci.* **281**, 458–464 (2005).
- <sup>20</sup>H. Kusumaatmaja *et al.*, *Langmuir* **24**, 7299–7308 (2008).
- <sup>21</sup>L. Zhu, Y. Xiu, J. Xu, P. A. Tamirisa, D. W. Hess, and C-P. Wong, *Langmuir* **21**, 11208–11212 (2005).
- <sup>22</sup>P. Roach, N. J. Shirtcliffe, and M. I. Newton, *Soft Matter* **4**, 224–240 (2008).
- <sup>23</sup>C. Corbella *et al.*, *Diamond Relat. Mater.* **19**, 1124–1130 (2010).
- <sup>24</sup>H.-S. Zhang and K. Komvopoulos, *J. Mater. Res.* **24**, 3038–3043 (2009).